LETTER • OPEN ACCESS

Achievement of ion temperatures in excess of 100 million degrees Kelvin in the compact high-field spherical tokamak ST40

OPEN ACCESS
IOP Publishing | International Atomic Energy Agency
Nuclear Fusion
Nucl. Fusion **63** (2023) 054002 (6pp)
https://doi.org/10.1088/1741-4326/acbec8

Letter

Achievement of ion temperatures in excess of 100 million degrees Kelvin in the compact high-field spherical tokamak ST40

S.A.M. McNamara[1,*], O. Asunta[1], J. Bland[1], P.F. Buxton[1], C. Colgan[1], A. Dnestrovskii[1], M. Gemmell[1], M. Gryaznevich[1], D. Hoffman[1], F. Janky[1], J.B. Lister[1], H.F. Lowe[1], R.S. Mirfayzi[1], G. Naylor[1], V. Nemytov[1], J. Njau[1], T. Pyragius[1], A. Rengle[1], M. Romanelli[1], C. Romero[1], M. Sertoli[1], V. Shevchenko[1], J. Sinha[1], A. Sladkomedova[1], S. Sridhar[1], Y. Takase[1], P. Thomas[1], J. Varje[1], B. Vincent[1], H.V. Willett[1], J. Wood[1], D. Zakhar[1], D.J. Battaglia[2], S.M. Kaye[2], L.F. Delgado-Aparicio[2], R. Maingi[2], D. Mueller[2], M. Podesta[2], E. Delabie[3], B. Lomanowski[3], O. Marchuk[4] and the ST40 Team[1]

[1] Tokamak Energy Ltd, Milton Park, Oxfordshire OX14 4SD, United Kingdom of Great Britain and Northern Ireland
[2] Princeton Plasma Physics Laboratory, Princeton, NJ 08543, United States of America
[3] Oak Ridge National Laboratory, Oak Ridge, TN 37831, United States of America
[4] Forschungszentrum Jülich GmbH, Institut für Energie- und Klimaforschung—Plasmaphysik, Partner of the Trilateral Euregio Cluster (TEC), 52425 Jülich, Germany

E-mail: steven.mcnamara@tokamakenergy.co.uk

Received 17 October 2022, revised 12 February 2023
Accepted for publication 24 February 2023
Published 17 March 2023

Abstract

Ion temperatures of over 100 million degrees Kelvin (8.6 keV) have been produced in the ST40 compact high-field spherical tokamak (ST). Ion temperatures in excess of 5 keV have not previously been reached in any ST and have only been obtained in much larger devices with substantially more plasma heating power. The corresponding fusion triple product is calculated to be $n_{i0}T_{i0}\tau_E \approx 6 \pm 2 \times 10^{18}\mathrm{m}^{-3}\mathrm{keVs}$. These results demonstrate for the first time that ion temperatures relevant for commercial magnetic confinement fusion can be obtained in a compact high-field ST and bode well for fusion power plants based on the high-field ST.

Keywords: ST40, high-field, spherical tokamak, compact

* Author to whom any correspondence should be addressed.

1. Introduction

Spherical tokamaks (STs) have several beneficial features which make them an attractive option for commercial fusion power production. STs have a plasma aspect ratio (the ratio of the major to minor radii of the plasma torus) of less than approximately two and exhibit enhanced stability properties [1], as well as displaying more favourable transport and confinement properties than those observed in large aspect ratio tokamaks [2]. Recent advances in the development of high-field magnets made from high temperature superconductor, combined with the fundamentally favourable properties of the ST, opens a route to smaller size and potentially reduced cost fusion power plants. Tokamak Energy Ltd, a private company based in Oxfordshire, UK, is developing commercial fusion power plants based on this approach.

Part of this development includes advancing the physics basis for the high-field ST towards commercial fusion using the ST40 tokamak. ST40 is a compact high-field ST with copper magnets. In this letter we describe results from ST40, demonstrating the achievement of central ion temperatures above 100 million degrees Kelvin (8.6 keV), which was the primary milestone for the recent phase of ST40 operations [3]. By injecting 1.6 MW of deuterium neutral beams into a deuterium plasma of volume 0.9 m^3, with plasma current $I_P = 0.6$ MA and on-axis toroidal magnetic field of $B_T = 1.9$ T, carbon ion temperatures of 9.2 keV were measured using a charge exchange recombination spectroscopy (CXRS) system where the most central line of sight measures slightly off the magnetic axis. This corresponds to a central impurity temperature of 9.8 keV inferred using diagnostic forward models and to a main ion temperature of 9.6 keV estimated using TRANSP [4]. The error of the CXRS measured value is below 5%, while the uncertainty of the inferred values for the central temperatures (impurity and hydrogenic) is below 10%. This is the highest ion temperature achieved so far in a ST or any tokamak of comparable size. Equivalent ion temperatures have only previously been obtained on devices with plasma volumes greater than fifteen times larger than ST40 and with substantially more plasma heating power [5]. For these ST40 discharges the fusion triple product is calculated to be $n_{i0}T_{i0}\tau_E \approx 6 \pm 2 \times 10^{18} \mathrm{m}^{-3}\mathrm{keVs}$.

These temperatures were achieved in hot-ion mode scenarios, where the ion temperature exceeds that of the electrons, typically by a factor of two or greater, $T_i \gg T_e$. Hot-ion modes have been explored in several conventional tokamaks [6–9] and recently in the Globus-M2 ST [10]. Hot-ion modes generally share common features of peaked density profiles, centralised ion heating, suppression of turbulence leading to improved ion confinement, and low ion-electron collisional coupling to minimise power transfer from the hotter ions to cooler electrons.

2. ST40 description

Typical ST40 plasma parameters are, major radius $R_{Geo} \approx 0.4$–0.5 m; aspect ratios between $A \approx 1.6$–1.9; plasma currents ranging from $I_P \approx 0.4$–0.8 MA and on-axis toroidal magnetics fields of $B_T \approx 1.5$–2.2 T. Plasma heating is provided by two neutral beams injected tangentially in the co-current direction that deliver approximately 0.9 MW at 55 kV and 0.7 MW at 24 kV when operated in deuterium. Plasma start-up is via merging compression (MC), where two high-voltage in-vessel poloidal field coils inductively initiate the plasma [11]. MC is a robust start-up scheme that allows direct access to high plasma currents without the use of the central solenoid. A modest central solenoid, providing approximately 200 mVs of inductive flux, is used to further increase the plasma current and sustain the current flat-top, which can last up to 200 ms.

ST40 is equipped with numerous diagnostics. A full set of magnetic field and flux sensors are used for real-time magnetic control and post-pulse magnetic reconstruction. The plasma position and shape are determined in real-time using an in-house reconstruction code, PFIT, which estimates the plasma current centroid position. Between shots, magnetics-only equilibrium reconstruction is produced with EFIT [12]. The electron density is measured using two interferometers, a sub millimetre (SMM) system operating at 1 mm and a near-infrared (NIR) system operating 1 μm + 1.5 μm, which measure along a radial and tangential midplane line of sight respectively. A visible survey spectrometer and line-filtered diodes (D_α, D_β, C-II, C-III, O-II, O-III) are used for low-Z impurity and Bremsstrahlung monitoring, and a tangential viewing soft x-ray (SXR) camera with 10 μm Be-window provides information on the radiated power. A 15-channel neutral particle analyser measuring neutral hydrogenic particle fluxes at energies between 1–41 keV provides information on the fast ion distribution function. High-resolution fast visible (10 kHz) and D_α (1 kHz) cameras view the main chamber and upper/lower divertors. An IR camera views the central column and parts of the divertor regions.

A high spectral resolution x-ray crystal spectrometer (XRCS) diagnostic [13], measures electron and ion temperatures in the core region across a single LOS viewing radially across the midplane and requires a small prefill puff of argon in every shot. The XRCS ion temperature is obtained from the He-like Argon resonance line w and its uncertainty reflects the line fitting error and the instrument function of the spectrometer. The electron temperature is obtained by comparing argon I_k/I_w and $I_{n=3}/I_w$ line ratios. A visible CXRS system [13], viewing the C-VI 529 nm $n = 8-7$ spectral line, measures ion temperature and toroidal rotation profiles along 6 lines of sight intersecting the 24 keV heating neutral beam.

3. High ion temperature scenario

Figure 1 shows waveforms of the main plasma parameters of an ST40 pulse designed to maximise the ion temperature in deuterium plasmas with deuterium neutral beam injection. MC was used to initiate the plasma and establish an approximately circular centre column limited plasma with $I_P = 0.45$ MA and $R_{Geo} = 0.40$ m at 10 ms.

MC was followed by a fast current ramp phase where the plasma current was increased at a rate of 4 MA s^{-1} to 0.57 MA

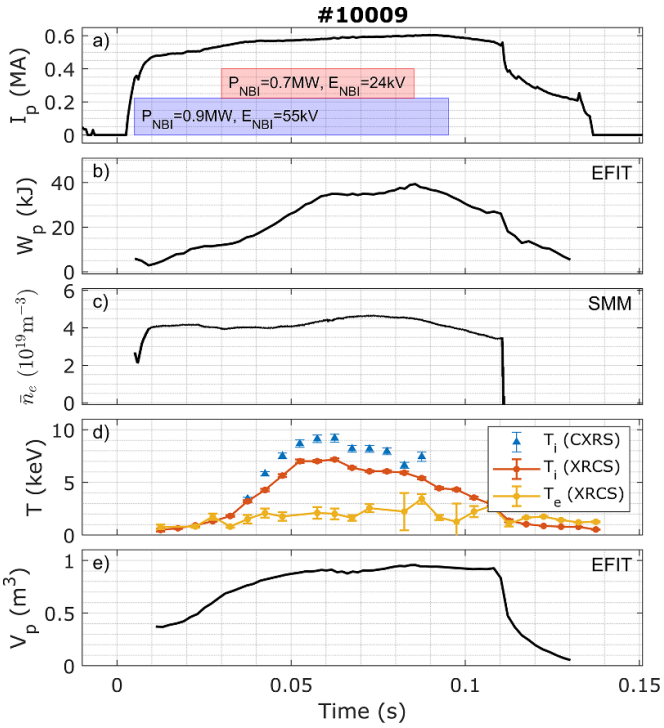

Figure 1. Overview of discharge #10009 designed to maximise central ion temperature. Shown are (*a*) plasma current and neutral beam injection parameters, (*b*) EFIT stored energy, (*c*) line averaged electron density; note an internal magnetic reconnection event (also visible on the plasma current and stored energy waveforms) occurs at 110 ms resulting in a loss of fringe count(s), (*d*) ion and electron temperature measured by the XRCS diagnostic and most centrally viewing chord of the CXRS system (with a measurement point tangency radius of 0.52 m compared to the EFIT magnetic axis at the time of maximum ion temperature of 0.51 m), and (*e*) plasma volume from EFIT magnetic reconstruction.

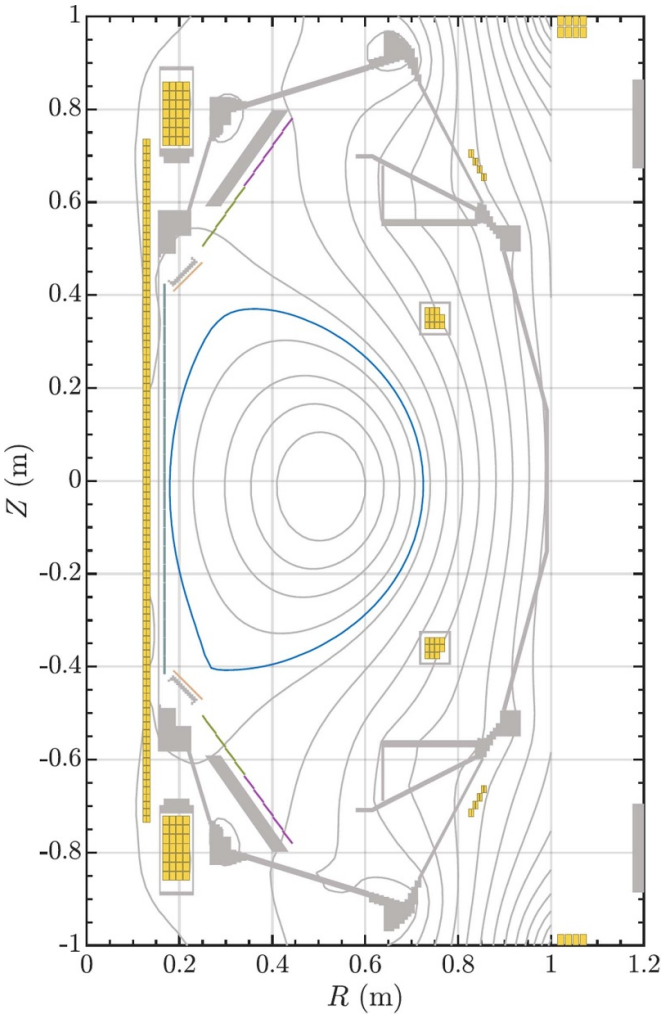

Figure 2. Plasma magnetic equilibrium reconstruction computed using EFIT at the time of maximum ion temperature for pulse #10009.

between 10–40 ms (figure 1(*a*)) using the central solenoid, while the plasma size was allowed to increase to $R_{\mathrm{Geo}} = 0.45$ m with an elongation $\kappa = 1.5$, aspect ratio $A = 1.65$, and plasma volume of $V_{\mathrm{p}} = 0.9$ m^3. At the end of the fast ramp the plasma is in a double null diverted configuration with a slight bias towards the lower divertor. The equilibrium shape is influenced by induced currents in a set of passive stabilisers mounted behind each divertor plate and around the upper and lower section of the centre column. A magnetic reconstruction at the time of maximum ion temperature is shown in figure 2. By this time the induced currents in the passive stabilisers have reduced and the plasma becomes marginally limited on the centre column, but with minimal interaction.

Injection of the 55 kV neutral beam began 5 ms before the start of the fast current ramp phase (figure 1(*a*)), which allowed the beam current to reach the maximum level by 10 ms, and together with the ohmic heating maintained a core electron temperature of around 1.5 keV, as measured using the XRCS diagnostic (figure 1(*d*)). The 55 kV beam fuelling maintained an approximately constant line averaged electron density of 4×10^{19} m^{-3} (figure 1(*c*)) without the need for gas puff fuelling, which would have resulted in a broadening of the density profile and neutral beam deposition profile. Because of this, gas puff fuelling was only used during plasma start-up. For obtaining the highest ion temperatures, the optimum line averaged electron density at the start of the 24 kV beam injection was found to be around 4×10^{19} m^{-3}. At this density, the ion-electron collisional coupling is sufficiently low and the fraction of absorbed beam power sufficiently high to enable access to hot-ion modes, with measured ion to electron temperature ratios of $T_i/T_e \approx 3-4$. The density after MC could be set by adjusting the pre-breakdown fuelling and duration of the intershot helium glow discharge cleaning (HeGDC). 5 min of intershot HeGDC was found to be sufficient to reduce the wall fuelling source from the graphite plasma facing components to a level where the target density could be achieved. Routine boronisations were also performed, which reduced impurity influx and substantially reduced the oxygen content and the Bremsstrahlung emission.

This high heating power phase started at 30 ms with the injection of the 24 kV beam (figure 1(*a*)), which remained on until 85 ms. During this phase, the plasma current was

gradually increased to 0.6 MA at a rate of approximately 0.6 MA s^{-1}. The combination of increased T_e, modest n_e, an increase in plasma cross-section and the fast plasma current ramp after MC all served to delay the onset of sawteeth, which otherwise limited the central ion temperature. Higher plasma currents of $I_P = 0.8$ MA were achieved during the programme. However, the optimum I_P for accessing high ion temperatures was found to be around 0.6 MA. Higher plasma currents advanced the onset of sawteeth and increased particle confinement resulting in higher densities, which led to a reduction in the peak ion temperature due to increased collisional coupling between ions and electrons. During both the plasma current ramp-up and high heating power phases the plasma remained in L-mode.

The injection of the 24 kV beam caused the ion temperature to increase rapidly (figure 1(*d*)). The argon impurity temperature measured by the XRCS increased from 1.5 keV to 7 keV in 25 ms. At its peak at 58 ms, the most centrally viewing chord of the CXRS diagnostic measured a carbon ion temperature of 9.2 keV by which point the stored energy had increased to 35 kJ. Due to its lower injection energy, this beam also provided more fuelling, resulting in an increase in the line averaged electron density to 4.5 x 10^{19} m^{-3} (figure 1(*c*)). This additional fuelling was during a period where the plasma volume was increasing (figure 1(*e*)), which offset the increase in the line averaged density. This increase in density reduced the measured ion temperature by around 1 keV and led to a ∼0.5 keV increase in electron temperature, due to the increased ion-electron coupling. The stored energy continued to rise, peaking at 40 kJ at the end of the high-power phase.

4. Interpretation of experimental results

Given the currently limited availability of profile data, the main plasma profile shapes have been constrained using an integrated analysis workflow. The workflow takes a wide range of parameterised profile shapes, including broad and peaked profiles, for the ion and electron temperatures, and the electron and impurity densities, and uses forward models to compute simulated measured quantities for each combination of profiles. These simulated quantities are then compared against the corresponding experimentally measured values. Profile combinations where the computed and measured values are in good agreement are retained, whilst the others rejected. This method allows the range of potential profile shapes to be constrained based the full set of available experimental measurements.

This workflow employs forward models of the XRCS [14], CXRS and interferometer diagnostics, makes use of ASTRA-NUBEAM [15, 16] to determine fast particle contributions, uses EFIT equilibrium reconstruction for remapping and to constrain the equilibrium stored energy, and computes the main ion temperatures from the impurity temperatures using TRANSP [4].

For the XRCS diagnostic, He-like Ar spectra have been modelled using atomic data [14], which includes all the relevant He and Li-like transitions. The CXRS diagnostic model uses FIDASIM [17] for the beam characterization and atomic data from OPEN-ADAS [18, 19] for the spectra, including cross-section effects in the calculation. Sensitivity studies and detailed experiments have shown that neither the XRCS or the CXRS are significantly affected by rotation shearing or temperature smearing and that the experimental measurements represent lower limits of the central values for the XRCS diagnostic and of the local values at the intersection between the lined of sight for the CXRS diagnostic and the neutral beam.

Using these models, the workflow proceeds as follows:

1. For each combination of profile shapes, the electron density profile is re-scaled to match the line of sight integral of the SMM interferometer and cross-checked versus the noisier NIR interferometer.
2. The electron temperature is scaled to match the experimental values of the argon I_k/I_w and $I_{n=3}/I_w$ line ratios measured by the XRCS and the ion temperature is scaled to match the XRCS measurement of the He-like Ar spectra.
3. For the impurities, the C and He concentrations are assumed to be constant across the radius and in time (at 3% and 1% respectively). The Ar concentration is set to follow the time evolution of the He-like w-resonance line, using a cross-calibration vs. Bremsstrahlung emission performed during dedicated pulses with and without Ar puffs. Values typically do not exceed $c_{Ar} \sim 0.1\%$. The trialled Ar density profile shapes include both flat and very peaked concentration profiles. The latter leads to more conservative estimates of the central temperatures from the XRCS weighing the emission shell further towards the plasma centre. Effects of impurity transport have been investigated but found to be of second order in comparison to the uncertainties in the profile shapes, which are accounted for in the model.
4. These scaled kinetic profiles are then fed into an interpretive ASTRA-NUBEAM simulation which calculates, amongst other things, the power balance, the fast particle pressure, total stored energy and loop voltage. The stored energy is compared with the value from EFIT, and if the modelled stored energy is within 20% of the measured value the profile combination is retained as a possible solution, otherwise it is discarded.
5. The remaining profile combinations are inputted into the CXRS forward model and only profile combinations where the simulated values are within ∼10% of the measured values are retained. The profile shape of the toroidal rotation is less well constrained due to systematic uncertainties in lines of sight and beam geometry, so the toroidal rotation profile uses the ion temperature parametrisation rescaled to central rotation value measured by the CXRS diagnostic.

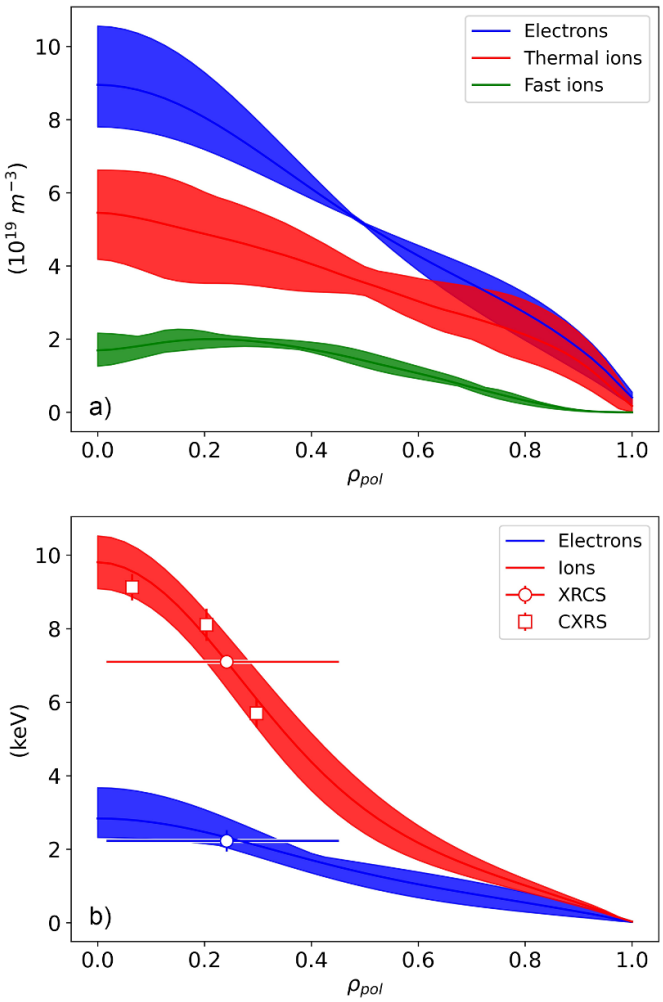

Figure 3. Profiles of (*a*) electron density, deuterium ion and fast ion densities, (*b*) deuterium ion and electron temperatures determined using the integrated analysis approach for pulse #10009 at time of maximum ion temperature (58 ms). Squares and circles in (*b*) are the measured temperatures from CXRS and XRCS, respectively, the horizontal line is the integration region of the XRCS measurement calculated as the 2nd moment of the He-like Ar resonance line emission shell.

6. Finally, TRANSP is used to calculate the thermal hydrogenic temperatures, which can differ from that of the measured impurities in plasmas with significant fast-particle fractions and low toroidal rotation. To account for the uncertainty in rotation speed, at 20% uncertainty is applied and independent TRANSP runs are performed at the lower and upper bounds of this range.

The resulting temperature and density profiles for pulse #10009 at the time of peak ion temperature, 58 ms, are shown in figure 3. The uncertainty band of the profiles, accounts for all the retained profile sets. The ion temperature profile is relatively well constrained in the inner half of the plasma by the three CXRS measurements (indicated by the red squares in figure 3(*b*)). These are localized in real space at the intersection between the spectrometer LOS and the neutral beam and provide a good constraint also for the XRCS measurement whose radial localisation depends on the emission position of the measured spectral line(s). Since the XRCS ion temperature value (red circle) fits well in-between the CXRS points and the emission distribution function is almost identical for the XRCS ion and electron temperature measurement, this reasonable radial localisation can be used also for the XRCS electron temperature value (blue circle). For the electron density profile, flat profiles are discarded as the resulting modelled stored energies would exceed the measured values. Additional indication of peaked density profiles come from peaked SXR profiles and sawtooth crashes that have been observed in other discharges with similar density, current and neutral beam heating power.

The fast particle density, calculated using ASTRA-NUBEAM (green profile in figure 3(*a*)), is around a factor of three lower than the thermal main ion density (red profile in figure 3(*a*)), the calculation of which includes dilution from the impurities. $Z_{\rm eff}$ is estimated to be approximately 2. The central toroidal rotation speed, as measured by the CXRS, is 220 km s^{-1}, with the lower and upper bounds used in the TRANSP runs taken as 160 km s^{-1} and 260 km s^{-1}. The resulting central deuterium temperature is, in both cases, only slightly lower than that of the impurities, with a value of 9.6 ± 0.4 keV for the high rotation case, which decreases by about 0.2 keV if low rotation is assumed.

For the range of profiles above, the total injected neutral beam power was 1.6 MW with 5%–8% shine through, the ohmic heating power was 0.5 MW and the fast ions account for approximately 30% of the stored energy. Taking these values of the absorbed neutral beam, $P_{\rm NB}$, and ohmic, $P_{\rm OH}$, heating powers and the thermal stored energy computed by ASTRA, $W_{\rm th}$, the energy confinement time, defined as $\tau_E = W_{\rm th}/(P_{\rm NB} + P_{\rm OH} - {\rm d}W_{\rm th}/{\rm d}t)$, is calculated to be 15 ms. The fusion triple product is calculated to be $n_{i0}T_{i0}\tau_E \approx 6 \pm 2 \times 10^{18}{\rm m}^{-3}{\rm keVs}$. Further analysis, using TRANSP, of the confinement properties of ST40 plasmas will be presented in [20].

5. Conclusions

We have reported on the attainment of central ion temperatures of 9.6 ± 0.4 keV and corresponding fusion triple product of $n_{i0}T_{i0}\tau_E \approx 6 \pm 2 \times 10^{18}{\rm m}^{-3}{\rm keVs}$ in the ST40 tokamak and demonstrated for the first time that ion temperatures relevant for commercial magnetic confinement fusion [21] can be achieved in a compact, high field, ST.

Acknowledgments

We gratefully acknowledge the hard work and dedication of the ST40 team; the support of the Tokamak Energy Board and shareholders; the guidance and scrutiny of the independent Diagnostics Advisory Board chaired by Alan Costley and

attended by Kieran Gibson, Patrick Carolan, Jo Lister, Manfred von Hellermann, Francesco Orsitto and Tom Todd; and the contributions from collaborators at Princeton Plasma Physics Laboratory and Oak Ridge National Laboratory that were supported through U.S. Department of Energy CRADA NFE-19-07769.

ORCID iDs

S.A.M. McNamara https://orcid.org/0000-0002-0477-5247
O. Asunta https://orcid.org/0000-0001-5618-5380
J. Bland https://orcid.org/0000-0002-4083-7812
P.F. Buxton https://orcid.org/0000-0002-0349-0434
C. Colgan https://orcid.org/0000-0001-6227-2317
A. Dnestrovskii https://orcid.org/0000-0002-4827-9421
M. Gemmell https://orcid.org/0009-0003-2469-3665
M. Gryaznevich https://orcid.org/0000-0002-4518-5593
D. Hoffman https://orcid.org/0000-0001-6898-7807
F. Janky https://orcid.org/0009-0001-9488-7188
H.F. Lowe https://orcid.org/0000-0001-6183-1383
R.S. Mirfayzi https://orcid.org/0000-0003-4628-796X
G. Naylor https://orcid.org/0009-0009-0279-4506
V. Nemytov https://orcid.org/0009-0007-6490-2635
T. Pyragius https://orcid.org/0000-0002-4388-2600
A. Rengle https://orcid.org/0009-0001-9037-1125
M. Romanelli https://orcid.org/0000-0003-4897-4843
C. Romero https://orcid.org/0009-0004-2032-5213
M. Sertoli https://orcid.org/0000-0003-1528-6307
V. Shevchenko https://orcid.org/0009-0007-4795-8717
J. Sinha https://orcid.org/0000-0002-9721-769X
A. Sladkomedova https://orcid.org/0000-0002-0012-9328
S. Sridhar https://orcid.org/0000-0002-7458-8092
Y. Takase https://orcid.org/0000-0002-4846-5267
J. Varje https://orcid.org/0000-0003-4137-2436
B. Vincent https://orcid.org/0009-0009-5293-444X
H.V. Willett https://orcid.org/0000-0002-4324-3438
J. Wood https://orcid.org/0009-0006-0391-2250
D. Zakhar https://orcid.org/0009-0006-6442-1367
D.J. Battaglia https://orcid.org/0000-0001-8897-9740
S.M. Kaye https://orcid.org/0000-0002-2514-1163
L.F. Delgado-Aparicio https://orcid.org/0000-0001-6739-4380
R. Maingi https://orcid.org/0000-0003-1238-8121
D. Mueller https://orcid.org/0000-0002-2456-3356
M. Podesta https://orcid.org/0000-0003-4975-0585
E. Delabie https://orcid.org/0000-0001-9834-874X
B. Lomanowski https://orcid.org/0000-0003-2226-2004
O. Marchuk https://orcid.org/0000-0001-6272-2605

References

[1] Peng Y.K.M. and Strickler D.J. 1986 Features of spherical torus plasmas *Nucl. Fusion* **26** 769
[2] Kaye S.M., Connor J.W. and Roach C.M. 2021 Thermal confinement and transport in spherical tokamaks: a review *Plasma Phys. Control. Fusion* **63** 123001
[3] Dnestrovskij A.Y., Connor J.W. and Gryaznevich M.P. 2019 On the confinement modeling of a high field spherical tokamak ST40 *Plasma Phys. Control. Fusion* **61** 055009
[4] Hawryluk R.J. 1981 An empirical approach to tokamak transport *Phys. Plasmas Close Thermonucl. Cond.* **1** 19
[5] Verdoolaege G. *et al* 2021 The updated ITPA global H-mode confinement database: description and analysis *Nucl. Fusion* **61** 076006
[6] Eubank H. *et al* 1979 Neutral-beam-heating results from the princeton large torus *Phys. Rev. Lett.* **43** 270
[7] Söldner F.X. *et al* 1999 Approach to steady state high performance in DD and DT plasmas with optimized shear in JET *Nucl. Fusion* **39** 407
[8] Mansfield D.K. *et al* 1996 Enhancement of tokamak fusion test reactor performance by lithium conditioning *Phys. Plasmas* **3** 1892
[9] Kishimoto H., Ishida S., Kikuchi M. and Ninomiya H. 2005 Advanced tokamak research on JT-60 *Nucl. Fusion* **45** 986
[10] Kurskiev G.S. *et al* 2022 The first observation of the hot ion mode at the globus-M2 spherical tokamak *Nucl. Fusion* **62** 104002
[11] Gryaznevich M.P. and Sykes A. 2017 Merging-compression formation of high temperature tokamak plasma *Nucl. Fusion* **57** 072003
[12] Lao L.L., St. John H., Stambaugh R.D., Kellman A.G. and Pfeiffer W. 1985 Reconstruction of current profile parameters and plasma shapes in tokamaks *Nucl. Fusion* **25** 1611
[13] Wood J. *et al* 2022 Characterisation of ion temperature and toroidal rotation on the ST40 tokamak *J. Instrum.* submitted
[14] Marchuk O. *et al* 2006 Comparison of impurity transport model with measurements of He-like spectra of argon at the tokamak TEXTOR *Plasma Phys. Control. Fusion* **48** 1633
[15] Pereverzev G.V. and Yushmanov P.N. 2002 *ASTRA. Automated System for Transport Analysis in a Tokamak* IPP (5/98) (Garching: Max-Planck-Institut für Plasmaphysik)
[16] Pankin A., McCune D., Andre R., Bateman G. and Kritz A. 2004 The tokamak Monte Carlo fast ion module NUBEAM in the National Transport Code Collaboration Library *Comput. Phys. Commun.* **159** 157
[17] Geiger B. *et al* 2020 Progress in modelling fast-ion D-alpha spectra and neutral particle analyzer fluxes using FIDASIM *Plasma Phys. Control. Fusion* **62** 105008
[18] Summers H. 2004 *The ADAS User Manual* Version 2.6 (available at: www.adas.ac.uk)
[19] OPEN-ADAS (available at: https://open.adas.ac.uk) (Accessed October 2022)
[20] Kaye S.M. *et al* 2022 Transport characteristics of high performance ST40 plasmas *Nucl. Fusion* submitted
[21] Wesson J. and Campbell D.J. 2011 *Tokamaks* 4th edn (Oxford: Oxford University Press)